

Proceeding Paper

# Spectrophotometric Determination of Amaranth Dye Using a Two-Step Green Cloud Point and Magnetic Solid-Phase Extraction Approach <sup>†</sup>

Remah A. Hassan and Zianab Tariq \*

Department of Chemistry, College of Science, University of Al-Qadisiyah, Diwaniya 58002, Iraq;  
sci.chem.mas.21.8@qu.edu.iq

\* Correspondence: zainab.tariq@qu.edu.iq

<sup>†</sup> Presented at the International Conference on Recent Advances in Science and Engineering, Dubai, United Arab Emirates, 4–5 October 2023.

**Abstract:** The present study introduces a two-step extraction methodology that integrates cloud point extraction (CPE) with magnetic solid-phase extraction (MSPE) for the extraction and quantification of amaranth dye. Initially, the dye is extracted using CPE in the micellar phase of the non-ionic surfactant Triton X-114. Subsequently, hydrophobic tetraethyl orthosilicate (TEOS)-modified Fe<sub>3</sub>O<sub>4</sub> magnetic nanoparticles (MNPs) are employed to recover the micellar phase. A comprehensive evaluation was conducted to optimize the key parameters influencing the efficacy of both CPE and MSPE techniques, as well as signal enhancement. Under optimized conditions, the proposed methodology exhibited a linear response in the concentration range of 10 to 90 µg Kg<sup>-1</sup>, with a correlation coefficient (*R*<sup>2</sup>) of 0.9945. The detection limit was determined to be 8.443 µg g<sup>-1</sup>. This robust and environmentally friendly approach offers a promising avenue for the accurate and efficient determination of amaranth dye in various applications.

**Keywords:** cloud point extraction (CPE); magnetic solid-phase extraction (MSPE); amaranth dye; spectrophotometric determination; magnetic nanoparticles (MNPs)



**Citation:** Hassan, R.A.; Tariq, Z. Spectrophotometric Determination of Amaranth Dye Using a Two-Step Green Cloud Point and Magnetic Solid-Phase Extraction Approach. *Eng. Proc.* **2023**, *59*, 244. <https://doi.org/10.3390/engproc2023059244>

Academic Editors: Nithesh Naik, Rajiv Selvam, Pavan Hiremath, Suhas Kowshik CS and Ritesh Ramakrishna Bhat

Published: 4 April 2024



**Copyright:** © 2024 by the authors. Licensee MDPI, Basel, Switzerland. This article is an open access article distributed under the terms and conditions of the Creative Commons Attribution (CC BY) license (<https://creativecommons.org/licenses/by/4.0/>).

## 1. Introduction

Amaranth (E-123) is a typical anionic azo dye extensively employed as a food coloring agent in various applications such as foodstuffs, cosmetics, medicines, synthetic fibers, and food additives. It is particularly used to give a vibrant red hue to various beverages. The excessive presence of amaranth azo dye in food products poses significant health risks, including genotoxicity, tumors, allergies, respiratory issues, and cytotoxicity [1,2]. The chemical structure is as shown in Figure 1.

Given these health implications, it is crucial to develop precise analytical methods for the determination of amaranth azo dye in food samples to ensure both food quality and consumer health safety. Several analytical techniques, including high-performance liquid chromatography (HPLC), voltammetry spectrometry, capillary electrophoresis, and electrochemical methods, have been widely employed for this purpose [3–9]. However, these methods often encounter two primary limitations: the first being the lower analytical sensitivity compared to the quantitative limits of the methods, and the second being the potential interference from other chemical species present in the samples. To address these issues, preconcentration techniques such as ion exchange (IE), solid-phase extraction (SPE), solvent extraction (SE), and cloud point extraction (CPE) have been utilized [10–20]. Cloud point extraction (CPE) is considered an environmentally friendly alternative to conventional liquid–liquid extraction (LLE) methods. It offers advantages such as a high enrichment factor, reduced usage of toxic reagents, smaller sample sizes, and the elimination of large volumes of organic solvents. Furthermore, it employs non-toxic surfactants, making the

method simpler, safer, and more economical [21]. Combining extraction methods can be advantageous in overcoming specific limitations inherent to individual techniques, thereby saving time and enhancing selectivity [22]. The objective of this study is to prepare  $\text{Fe}_3\text{O}_4$  nanocomposites, encapsulate them with tetraethyl orthosilicate (TEOS), and utilize them as adsorbents to improve the extraction efficiency of amaranth dye under optimized conditions of acidity, time, and temperature required for cloud point extraction.

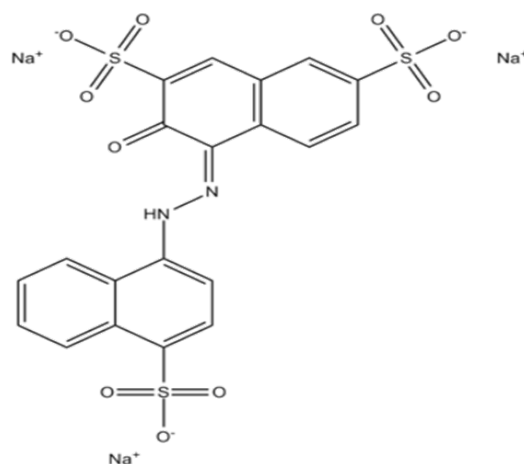


**Figure 1.** Chemical structure of amaranth.

## 2. Materials and Methods

### 2.1. Apparatus

A Jasco 7850 UV–Visible Spectrophotometer equipped with a 1 cm (0.5 mL) quartz cell was utilized for recording the absorption spectrum and absorption measurements. To expedite the phase separation process, a 3D device operating at 4000 rpm from UromAzma Corporation was employed. pH measurements were conducted using a Metrohm 632 pH meter with an integrated glass pH electrode. All measurements were carried out at the University of Al-Qadisiyah.

### 2.2. Chemicals

No additional purification was required for any of the chemicals and reagents used in this study. The azo dye, amaranth, also known as trisodium 2-hydroxy-1-(4-sulphonato-1-naphthylazo)naphthalene-3,6-disulphonate (molecular formula  $\text{C}_{20}\text{H}_{11}\text{N}_2\text{O}_{10}\text{S}_3\text{Na}_3$ , molecular weight 604), was purchased from M/s Merck. A 0.1g sample of the dye was weighed and dissolved in 10 mL of ethanol in a 100 mL volumetric flask. The volume was then made up to 100 mL with distilled water to prepare a stock solution of 1000 mg/L amaranth. Distilled water was used consistently throughout the study. For the absorbance measurements of amaranth dye solutions, a Shimadzu UV-1601PC spectrophotometer set at a wavelength of 520 nm was employed.

### 2.3. Synthesis of TEOS Functionalized Magnetic Nanoparticles

Magnetic nanoparticles (MNPs) were synthesized using the chemical co-precipitation method.  $\text{FeCl}_3 \cdot 6\text{H}_2\text{O}$  (11.68 g) and  $\text{FeCl}_2 \cdot 4\text{H}_2\text{O}$  (4.30 g) were dissolved in 200 mL of deionized water under a nitrogen atmosphere and stirred vigorously at 85 °C. Subsequently, 20 mL of 25% aqueous ammonia solution was added, causing the solution color to change from orange to black instantaneously. The magnetic precipitate was washed twice with deionized water and once with 0.02 mol  $\text{L}^{-1}$  sodium chloride solution. The resulting magnetic suspension was transferred to a 250 mL round-bottom flask and allowed to settle. A strong external magnet was used to isolate the  $\text{Fe}_3\text{O}_4$  nanoparticles, and the supernatant was discarded. The MNPs were then coated with TEOS by adding an aqueous solution of TEOS (10%, v/v, 80 mL) and glycerol (60 mL). The mixture was stirred and heated at 90 °C for 2 h under a nitrogen atmosphere.

Finally, the modified nanoparticles (TEOS-Fe<sub>3</sub>O<sub>4</sub>) were washed with deionized water (3 × 250 mL), methanol (2 × 150 mL), and deionized water (3 × 250 mL) before being dried as black powders in a vacuum oven at 45 °C for 2 h [23].

#### 2.4. Recommended Extraction Procedure

In a 10 mL test tube, 2 mL of 10 mg/L amaranth dye solution was combined with 2 mL of the surfactant Triton X-114 and 1 mL of a buffer solution at pH 3. The volume was then made up to the mark with ion-free distilled water. The test tube was placed in a water bath at 40 °C for 15 min until turbidity formed. Subsequently, the tube was centrifuged for 3 min to separate the organic layer from the aqueous layer. The organic layer was then collected, and 0.05 g of the nanomaterial was added. The mixture was sonicated for 5 min, after which the nanomaterial was removed using a magnet. Two mL of ethanol was added, and the solution was sonicated for an additional 15 min. Absorbance measurements were taken at a wavelength of 520 nm. A blank was prepared in a similar manner but without the presence of dye.

### 3. Result and Discussion

#### 3.1. Fourier Transform Infrared Spectroscopy (FTIR) Analysis

FTIR analysis was conducted for both unmodified Fe<sub>3</sub>O<sub>4</sub> magnetic nanoparticles and TEOS-modified Fe<sub>3</sub>O<sub>4</sub> magnetic nanoparticles. For the unmodified Fe<sub>3</sub>O<sub>4</sub> nanoparticles, the FTIR spectrum was obtained using the KBr (potassium bromide) disc method and is depicted in Figure 2. The spectrum was recorded within the wavenumber range of 400–4000 cm<sup>-1</sup>. The FTIR data for the unmodified Fe<sub>3</sub>O<sub>4</sub> nanoparticles are presented in Figure 2 and Table 1 which serves as a baseline for comparing the effects of TEOS modification.

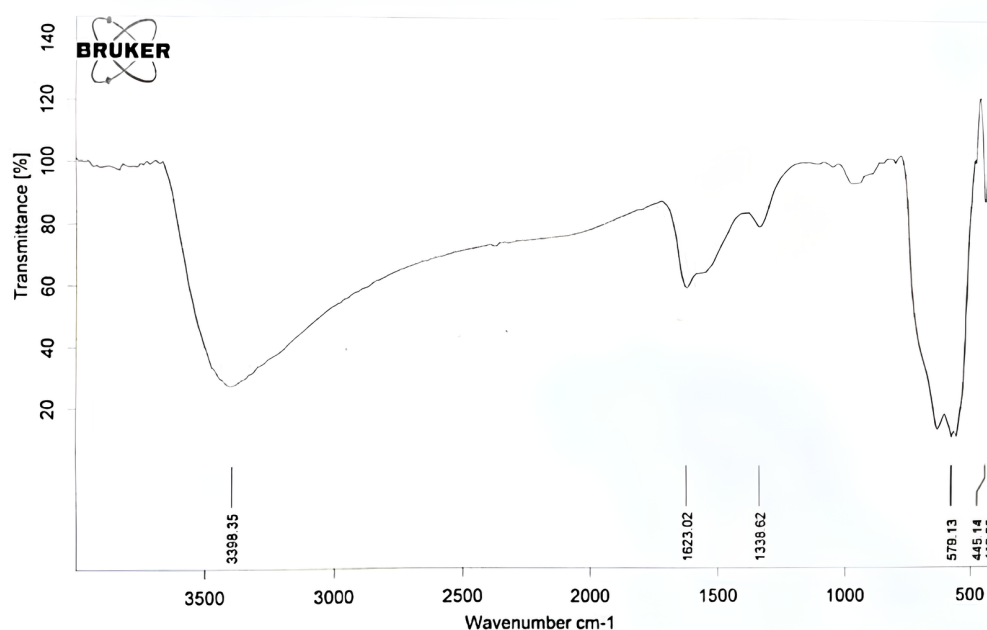


**Figure 2.** Infrared spectrum of Fe<sub>3</sub>O<sub>4</sub> nanoparticles before TEOS modification.

**Table 1.** Infrared spectrum data (400–4000 cm<sup>-1</sup>) for Fe<sub>3</sub>O<sub>4</sub>.

Wave Number (cm <sup>-1</sup> )	IR Bond
3398	O-H
1623	O-Fe-O
579	Fe-O

The wave numbers observed for  $\text{Fe}_3\text{O}_4$  are contingent upon the spectroscopic technique employed for analysis. Infrared spectroscopy is frequently used to study the vibrational modes of molecules, with wave numbers typically reported in units of reciprocal centimeters ( $\text{cm}^{-1}$ ). The infrared spectrum of  $\text{Fe}_3\text{O}_4$  generally exhibits several bands in the range of  $400\text{--}4000\text{ cm}^{-1}$ , corresponding to different vibrational modes within the iron oxide lattice. These wave numbers can vary based on sample preparation and measurement conditions. Some typical wave numbers for  $\text{Fe}_3\text{O}_4$  in the infrared region include

- $579\text{ cm}^{-1}$ : stretching vibration of Fe-O bonds.
- $670\text{ cm}^{-1}$ : bending vibration of Fe-O bonds (not observed in this study).
- $1100\text{--}1200\text{ cm}^{-1}$ : stretching vibration of the O-Fe-O bridges in the spinel structure (not observed in this study).
- $1623\text{ cm}^{-1}$ : bending vibration of the O-Fe-O bridges in the spinel structure.
- $3398\text{ cm}^{-1}$ : O-H stretching, associated with water molecules adsorbed on the surface of  $\text{Fe}_3\text{O}_4$ .

Note that these wave numbers are approximate and may vary depending on the specific sample.

The FTIR data for  $\text{Fe}_3\text{O}_4$  nanoparticles after TEOS coating are presented in Table 2 and Figure 3. The spectrum reveals several new peaks compared to the uncoated  $\text{Fe}_3\text{O}_4$ , indicating successful modification. Notably, the appearance of peaks at  $1058\text{ cm}^{-1}$  and  $850\text{ cm}^{-1}$  can be attributed to Si-O-Si and  $\text{CH}_3\text{-Si-O-}$  bonds, respectively, confirming the presence of TEOS on the  $\text{Fe}_3\text{O}_4$  surface.

**Table 2.** FTIR data for  $\text{Fe}_3\text{O}_4$  nanoparticles after TEOS coating.

Wave Number ( $\text{cm}^{-1}$ )	IR Bond
3399	O-H stretching
1539	O-H bending
1058	Si-O-Si
850	$\text{CH}_3\text{-Si-O-}$
2923	CH-
588–465	Fe-O
875	Si-O-C

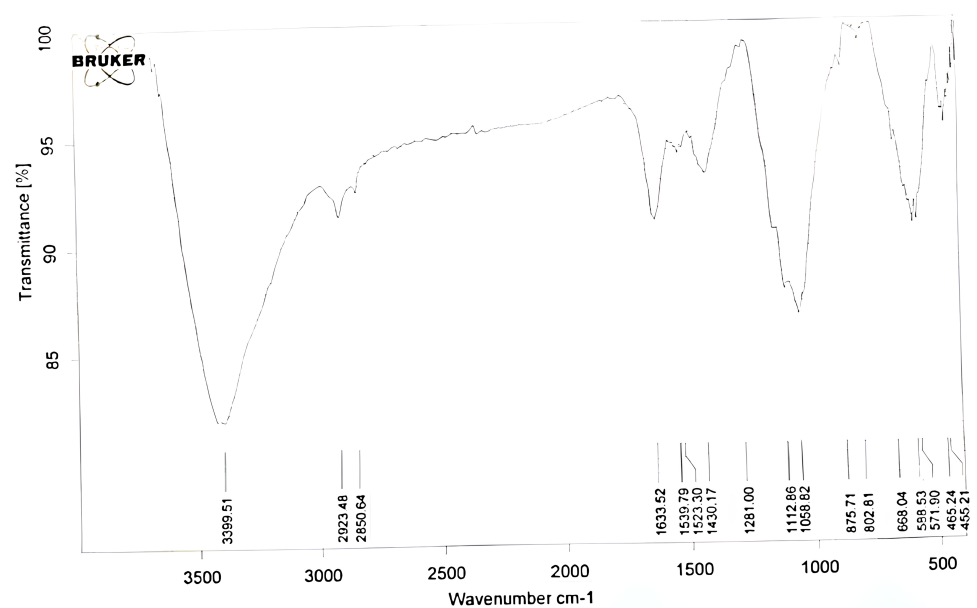


**Figure 3.** FT-IR spectrum of  $\text{Fe}_3\text{O}_4$  nanoparticles coated with TEOS.

The FTIR spectrum of TEOS-coated  $\text{Fe}_3\text{O}_4$  is expected to contain absorption peaks corresponding to both TEOS and  $\text{Fe}_3\text{O}_4$ , as well as any functional groups that may be present on the surface of the nanoparticles. Below are some typical FTIR wavenumbers for TEOS and  $\text{Fe}_3\text{O}_4$ :

(A) **TEOS:**

- $1058\text{ cm}^{-1}$ : Si-O-Si stretching;
- $875\text{ cm}^{-1}$ : Si-O-C stretching;
- $850\text{ cm}^{-1}$ : Si-O- $\text{CH}_3$  bending;
- $2923\text{ cm}^{-1}$ : C-H stretching of ethyl groups.

(B)  **$\text{Fe}_3\text{O}_4$ :**

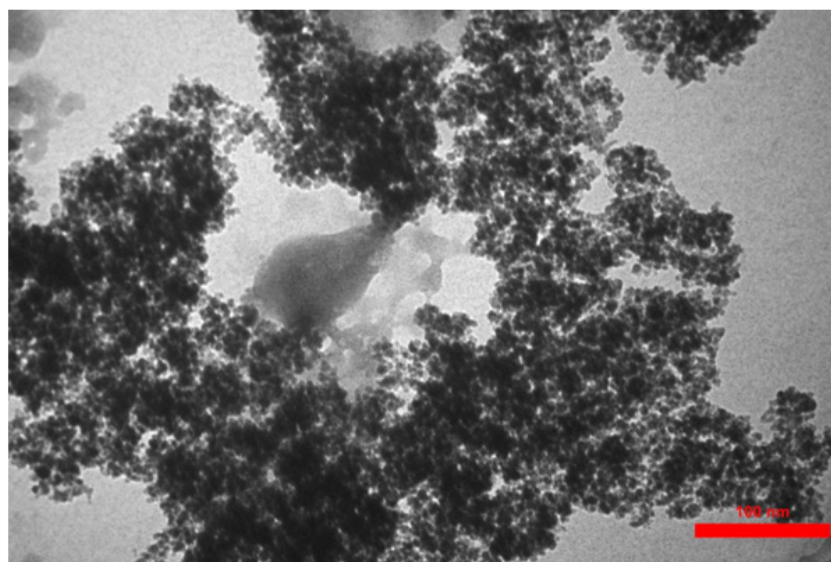
- $588\text{--}465\text{ cm}^{-1}$ : Fe-O stretching;
- $1539\text{ cm}^{-1}$ : O-H bending (associated with water molecules on the surface of  $\text{Fe}_3\text{O}_4$ );
- $3399\text{ cm}^{-1}$ : O-H stretching (associated with water molecules on the surface of  $\text{Fe}_3\text{O}_4$ ).

Note that the exact wavenumbers and peak shapes can vary depending on factors such as the synthesis method, the size and shape of the nanoparticles, and any surface modifications that may have been applied.

### 3.2. Transmission Electron Microscopy (TEM)

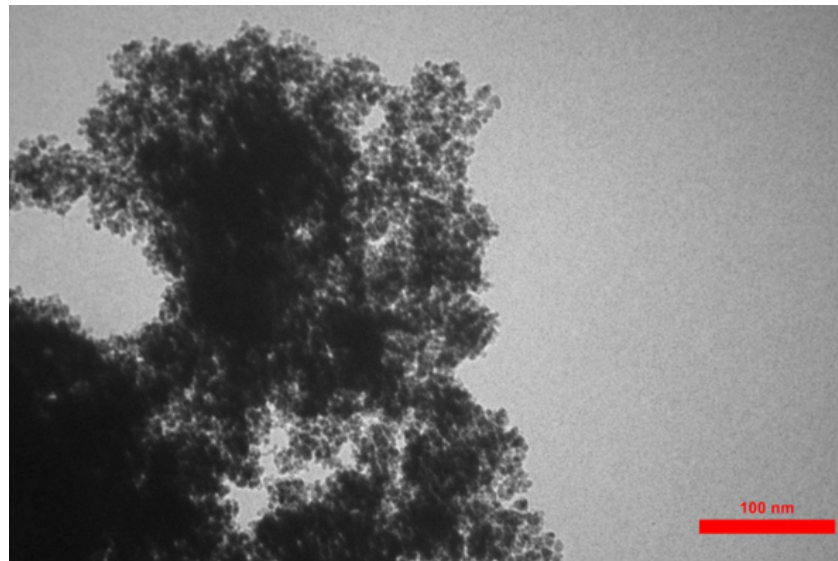
Transmission Electron Microscopy (TEM) offers highly detailed insights into the structure and composition of materials, including aspects such as crystal structure, defects, grain boundaries, and surface features.

Figure 4 presents the TEM analysis of  $\text{Fe}_3\text{O}_4$  nanoparticles. The particles were observed to have a size range of 50–100 nm and were nearly spherical in shape, consistent with previous studies.



**Figure 4.** Transmission Electron Microscopy image of  $\text{Fe}_3\text{O}_4$  nanoparticles.

Upon coating  $\text{Fe}_3\text{O}_4$  with TEOS, a distinct change in morphology was observed, as shown in Figure 5. The dark-colored nanoparticles represent the  $\text{Fe}_3\text{O}_4$  core, while the lighter-colored particles indicate the TEOS coating. The image reveals that the TEOS surface is densely covered by uniformly distributed  $\text{Fe}_3\text{O}_4$  nanoparticles, indicating a significant agglomeration of  $\text{Fe}_3\text{O}_4$  particles on the TEOS surface.



**Figure 5.** Transmission Electron Microscopy image of TEOS-coated  $\text{Fe}_3\text{O}_4$  nanoparticles.

### 3.3. X-Ray Diffraction (XRD)

X-ray diffraction (XRD) provides valuable insights into the crystal structure and particle size of materials. The XRD pattern of  $\text{Fe}_3\text{O}_4$  nanoparticles exhibited main diffraction peaks at  $2\theta$  angles of approximately  $30.1^\circ$ ,  $35.5^\circ$ ,  $43.1^\circ$ ,  $53.7^\circ$ ,  $57.3^\circ$ , and  $62.8^\circ$ . These peaks correspond to the (220), (311), (400), (422), (511), and (440) planes of the cubic spinel crystal structure of  $\text{Fe}_3\text{O}_4$ .

The intensity and full-width at half maxima (FWHM) of these peaks can provide information about the size and degree of crystallinity of the  $\text{Fe}_3\text{O}_4$  nanoparticles (Figure 6). Smaller particle sizes result in broader diffraction peaks and lower peak intensity. Peak broadening may also indicate a degree of disorder within the crystalline structure of the nanoparticles. In the XRD spectrum of  $\text{Fe}_3\text{O}_4$ -TEOS nanocomposites (Figure 7), two sets of diffraction peaks were observed. The first set, similar to that of pure  $\text{Fe}_3\text{O}_4$ , corresponds to its crystalline phase. The second set shows a broad hump at  $2\theta$  angles around  $20^\circ$ – $25^\circ$ , representing the amorphous phase of TEOS.

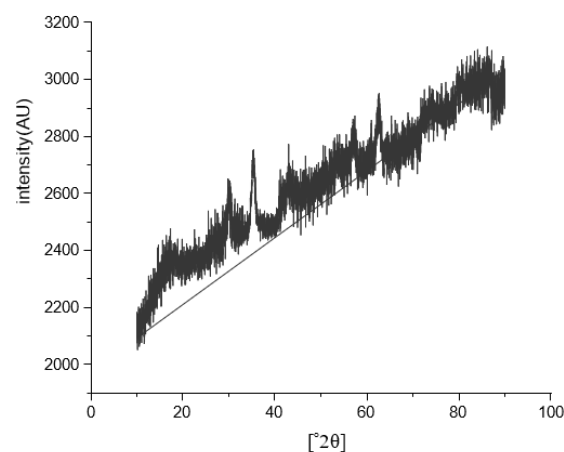


**Figure 6.** X-ray diffraction spectrum of  $\text{Fe}_3\text{O}_4$  nanoparticles.

Overall, the XRD spectrum of  $\text{Fe}_3\text{O}_4$ -TEOS nanocomposites confirms the presence of both crystalline and amorphous phases, suggesting that the nanocomposites comprise both crystalline and non-crystalline regions. The relative intensity of the peaks for each component can offer insights into the composition and morphology of the nanocomposites.

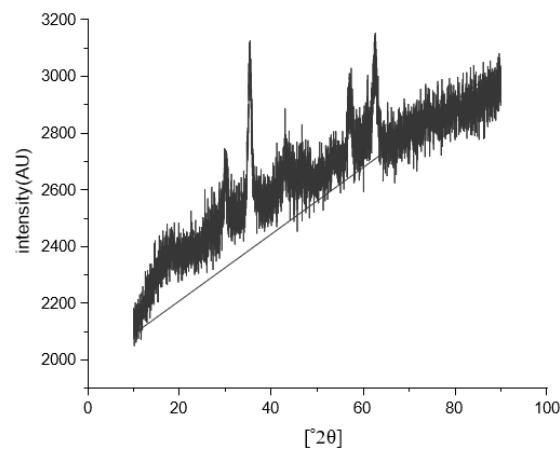


**Figure 7.** X-ray diffraction spectrum of  $\text{Fe}_3\text{O}_4$  nanoparticles coated with TEOS.

### 3.4. Optimization of CPE Procedure

#### 3.4.1. Effect of pH

The influence of pH, ranging from 2 to 9, was investigated using various acetate buffer solutions. The results are depicted in Figure 8. At pH 3, maximum absorption was observed. Subsequent increases in pH led to decreased absorption due to partial dissociation at higher pH levels. Therefore, pH 3 was selected as the optimal pH for dye adsorption at the wavelength of maximum absorption, 520 nm.

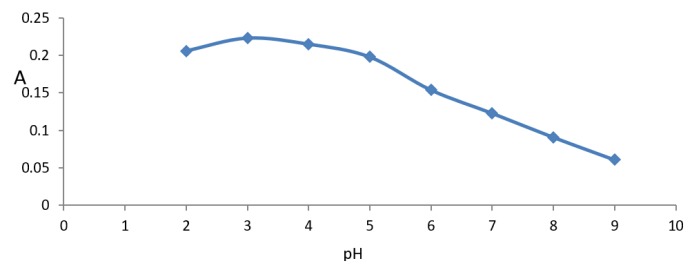


**Figure 8.** Effect of pH on the adsorption of the organic layer of amaranth dye. Conditions: 1 mL of dye, 2 mL of Triton X-114.

#### 3.4.2. Effect of Time

The optimal time for measuring dye absorbance was investigated over a range from 5 to 25 min using Triton X-114 solution. The results are presented in Figure 9. Absorption initially increased with time, peaking at 15 min, and then decreased due to partial dissociation at longer times. Consequently, 15 min was chosen as the optimal time for measuring absorbance at 520 nm.

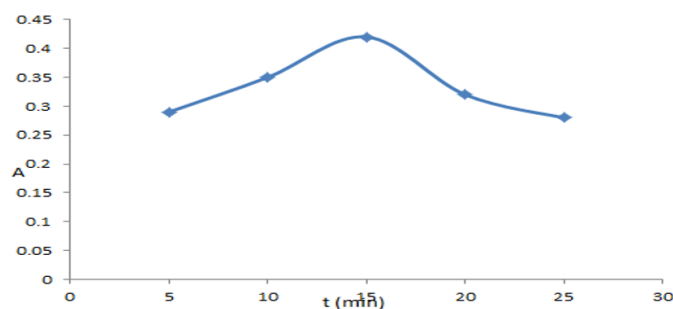


**Figure 9.** The effect of time on the adsorption of the organic layer of amaranth dye. Conditions: 2 mL of dye, 2 mL of Triton X-114, pH 3.

### 3.4.3. Effect of Temperature

The impact of temperature, ranging from 30 to 90 °C, was studied using solutions of dye and Triton X-114. As shown in Figure 10, absorption initially increased with temperature, reaching a peak at 40 °C. Beyond this point, absorption decreased due to partial dissociation at higher temperatures. Therefore, 40 °C was selected as the optimal temperature for dye adsorption at 520 nm.

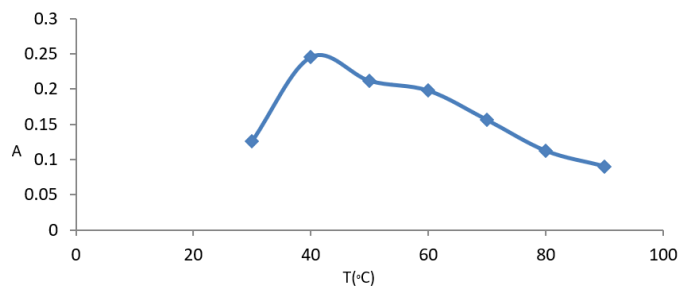


**Figure 10.** The effect of temperature on the adsorption of the organic layer of amaranth dye. Conditions: 2 mL of dye, 2 mL of Triton X-114, pH 3, temperature 40 °C, time 15 min.

### 3.4.4. Effect of Amount of Nanomaterials

TEOS-modified Fe<sub>3</sub>O<sub>4</sub>-NPs were added to the sample solution in amounts ranging from 0.01 to 0.06 g. As shown in Figure 11, the extraction efficiency improved up to 0.05 g of adsorbent. Due to the high surface-to-volume ratio of the nanoparticles, accurate extraction could be achieved with a minimal amount of adsorbent. Consequently, 0.05 g was selected for further experiments.

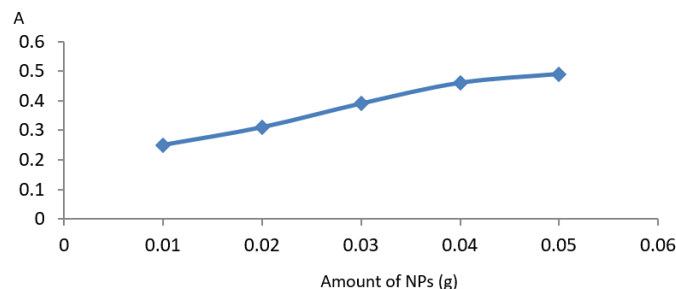


**Figure 11.** The effect of the amount of nano material on the adsorption of the organic layer of the dye. Conditions: 2 mL of dye, 2 mL of Triton X-114, pH 3, temperature 40 °C, time 15 min.

### 3.4.5. Analytical Performance of the Optimized Method

Under optimal conditions, the calibration curve was linear over a concentration range of 10–90 µg Kg<sup>-1</sup> with a correlation coefficient ( $R^2$ ) of 0.9945. Calibration curve solutions were prepared by spiking appropriate amounts of amaranth dye working solutions and subjected to the recommended CPE-MSPE procedure. The limit of detection (LOD), calculated as  $3.3 \times S_b / m$  (where  $S_b$  is the standard deviation of nine replicate measurements of a blank solution, and  $m$  is the slope of the calibration curve), was found to be 8.443 µg g<sup>-1</sup>.

## 4. Conclusions

The integration of Cloud Point Extraction (CPE) with Tetraethyl Orthosilicate (TEOS)-modified Fe<sub>3</sub>O<sub>4</sub> Magnetic Solid-Phase Extraction (MSPE) has been effectively utilized as a proficient sample pretreatment procedure for the extraction and determination of amaranth dye. This analytical methodology offers several advantages such as operational simplicity, minimal organic solvent consumption, and a high pre-concentration factor. Furthermore, the developed approach demonstrates a competent capability for the detection of trace amounts of amaranth dye in various samples, showcasing its potential applicability in ensuring the quality and safety of products containing amaranth dye.

**Author Contributions:** Methodology and writing—original draft preparation, Z.T.; validation, R.A.H.; formal analysis, R.A.H.; investigation, R.A.H.; resources, R.A.H.; data curation, R.A.H.; writing—review and editing, Z.T. All authors have read and agreed to the published version of the manuscript.

**Funding:** This research received no external funding.

**Institutional Review Board Statement:** Not applicable.

**Informed Consent Statement:** Not applicable.

**Data Availability Statement:** All the data used in the experiment has been made available in the present article.

**Conflicts of Interest:** The authors declare no conflicts of interest.

## References

1. Puzenat, E.; Lachheb, H.; Karkmaz, M.; Houas, A.; Guillard, C.; Herrmann, J.M. Fate of nitrogen atoms in the photocatalytic degradation of industrial (congo red) and alimentary (amaranth) azo dyes. Evidence for mineralization into gaseous dinitrogen. *Int. J. Photoenergy* **2003**, *5*, 51–58. [[CrossRef](#)]
2. Christodoulou, P.; Kareli, D.; Poliliou, S. Cytogenetic evaluation and DNA interaction studies of the food colorants amaranth, erythrosine and tartrazine. *Food Chem. Toxicol.* **2010**, *48*, 2944–2934.
3. Ma, M.; Luo, X.; Chen, B.; Su, S.; Yao, S. Simultaneous determination of water-soluble and fat-soluble synthetic colorants in foodstuff by high-performance liquid chromatography–diode array detection–electrospray mass spectrometry. *J. Chromatogr. A* **2006**, *1103*, 170–176. [[CrossRef](#)] [[PubMed](#)]
4. Ghanbari, P.K.; Roushani, M.; Farzadfar, F.; Goicoechea, H.; Jalalvand, A.R. Developing a four-dimensional voltammetry as a powerful electroanalytical methodology for simultaneous determination of three colorants in the presence of an uncalibrated interference. *Chemom. Intell. Lab. Syst.* **2019**, *189*, 27–38. [[CrossRef](#)]
5. Ahmadh, A. A Square-Wave Adsorptive Stripping Voltammetric Method for the Determination of Amaranth, a Food Additive Dye. *J. AOAC Int.* **2005**, *88*, 788–793.
6. Rývolová, M.; Táborský, P.; Vrábek, P.; Krásenský, P.; Preisler, J. Sensitive determination of erythrosine and other red food colorants using capillary electrophoresis with laser-induced fluorescence detection. *J. Chromatogr. A* **2007**, *1141*, 206–211. [[CrossRef](#)] [[PubMed](#)]
7. Wang, P.; Hu, X.; Cheng, Q.; Zhao, X.; Fu, X.; Wu, K. Electrochemical detection of amaranth in food based on the enhancement effect of carbon nanotube film. *J. Agric. Food Chem.* **2010**, *58*, 12112–12116. [[CrossRef](#)] [[PubMed](#)]
8. Pogacean, F.; Rosu, M.-C.; Coros, M.; Magerusan, L.; Moldovan, M.; Sarosi, C. Graphene/TiO<sub>2</sub>-Ag based composites used as sensitive electrode materials for amaranth electrochemical detection and degradation. *J. Electrochem. Soc.* **2018**, *165*, 3054–3059. [[CrossRef](#)]
9. Liu, L.; Mi, Z.; Li, H.; Li, C.; Hu, Q.; Feng, F. Highly selective and sensitive detection of amaranth by using carbon dots-based nanosensor. *RSC Adv.* **2019**, *9*, 26315–26320. [[CrossRef](#)] [[PubMed](#)]
10. Xia, X.; Zhu, C.; Luo, J.; Zeng, Z.; Guan, C.; Ng, C.F.; Fan, H.J. Synthesis of Free-Standing Metal Sulfide Nanoarrays via Anion Exchange Reaction and Their Electrochemical Energy Storage Application. *Small* **2014**, *10*, 766–773. [[CrossRef](#)] [[PubMed](#)]
11. Hong, J.G.; Zhang, B.; Glabman, S.; Uzal, N.; Dou, X.; Zhang, H.; Chen, Y. Potential ion exchange membranes and system performance in reverse electrodialysis for power generation: A review. *J. Membr. Sci.* **2015**, *486*, 71–88. [[CrossRef](#)]
12. Qi, P.; Zeng, T.; Wen, Z.; Liang, X.; Zhang, X. Interference-free simultaneous determination of Sudan dyes in chili foods using solid phase extraction coupled with HPLC–DAD. *Food Chem.* **2011**, *125*, 1462–1467. [[CrossRef](#)]
13. Soyak, M.; Unsal, Y.E.; Yilmaz, E.; Tuzen, M. Determination of rhodamine B in soft drink, waste water and lipstick samples after solid phase extraction. *Food Chem. Toxicol.* **2011**, *49*, 1796–1799. [[CrossRef](#)] [[PubMed](#)]
14. Zaghdoudi, K.; Pontvianne, S.; Framboisier, X.; Achard, M.; Kudaibergenova, R.; Ayadi-Trabelsi, M.; Guiavarc, Y. Accelerated solvent extraction of carotenoids from: Tunisian Kaki (*Diospyros kaki* L.), peach (*Prunus persica* L.) and apricot (*Prunus armeniaca* L.). *Food Chem.* **2015**, *184*, 131–139. [[CrossRef](#)] [[PubMed](#)]
15. Altunay, N.; Gürkan, R. A new cloud point extraction procedure for determination of inorganic antimony species in beverages and biological samples by flame atomic absorption spectrometry. *Food Chem.* **2015**, *175*, 507–515. [[CrossRef](#)] [[PubMed](#)]
16. Gürkan, R.; Korkmaz, S.; Altunay, N. Preconcentration and determination of vanadium and molybdenum in milk, vegetables and foodstuffs by ultrasonic-thermostatic-assisted cloud point extraction coupled to flame atomic absorption spectrometry. *Talanta* **2016**, *155*, 38–46. [[CrossRef](#)] [[PubMed](#)]
17. Altunay, N.; Gürkan, R.; Orhan, U. A new ultrasonic-assisted cloud-point-extraction procedure for pre-concentration and determination of ultra-trace levels of copper in selected beverages and foods by flame atomic absorption spectrometry. *Food Addit. Contam. Part A* **2015**, *32*, 1475–1487. [[CrossRef](#)] [[PubMed](#)]
18. Elik, A.; Altunay, N.; Gürkan, R. Determination of trace levels of nitrite in beverages samples through micellar improved catalytic kinetic spectrophotometry. *Cumhuriyet Sci. J.* **2017**, *38*, 400–411. [[CrossRef](#)]

19. Mpountoukas, P.; Pantazaki, A.; Kostareli, E.; Sha, O.; Zhu, X.; Feng, Y.; Ma, W. Aqueous two-phase based on ionic liquid liquid–liquid microextraction for simultaneous determination of five synthetic food colourants in different food samples by high-performance liquid chromatography. *Food Chem.* **2015**, *174*, 380–386.
20. Wang, M.; Sun, Y.; Yang, X.; Zhao, J. Sensitive determination of amaranth in drinks by highly dispersed cnt in graphene oxide “water” with the aid of small amounts of ionic liquid. *Food Chem.* **2015**, *179*, 318–324. [[CrossRef](#)] [[PubMed](#)]
21. Gürkan, R.; Altunay, N. Quantification of 5-hydroxymethylfurfural in honey samples and acidic beverages using spectrophotometry coupled with ultrasonic-assisted cloud point extraction. *J. Food Compos. Anal.* **2015**, *42*, 141–151. [[CrossRef](#)]
22. Cruz-Vera, M.; Lucena, R.; Cárdenas, S.; Valcárcel, M. Sample Treatments Based on Dispersive (Micro)Extraction. *Anal. Methods* **2011**, *3*, 1719–1728. [[CrossRef](#)]
23. Mahdi, H.; Zohreh, T.; Sara, P.; Mohammad, T. Spectrofluorimetric determination of zearalenone using dispersive liquid–liquid microextraction coupled to micro-solid phase extraction onto magnetic nanoparticles. *RSC Adv.* **2014**, *4*, 45065–45073.

**Disclaimer/Publisher’s Note:** The statements, opinions and data contained in all publications are solely those of the individual author(s) and contributor(s) and not of MDPI and/or the editor(s). MDPI and/or the editor(s) disclaim responsibility for any injury to people or property resulting from any ideas, methods, instructions or products referred to in the content.